mater.scichina.com link.springer.com

Published online 21 September 2022 | https://doi.org/10.1007/s40843-022-2176-6
Sci China Mater 2023, 66(2): 541–555

Molecular engineering toward sustainable development of multiple-doped hierarchical porous carbons for superior zinc ion storage

Mingquan Liu[1,2], Feng Wu[1,2], Xin Feng[1], Yahui Wang[1,2], Lumin Zheng[1], Xin Li[3], Ying Li[1], Yuteng Gong[1], Ying Bai[1*] and Chuan Wu[1,2*]

ABSTRACT **Aqueous Zn-ion hybrid supercapacitors (ZHSCs) hold great potential as next-generation energy storage devices due to their low cost, excellent rate capability, long cycling life, and high safety. Heteroatom-doped hierarchical porous carbons (HD-HPCs) with integrated high specific surface area, multiscale pores, and abundant defects have been regarded as promising cathode materials for ZHSCs. However, the *in situ* architecture of HD-HPCs with these multiple advantages *via* a sustainable and controllable method remains an arduous challenge. Herein, a novel molecular engineering strategy was proposed for the *in situ* construction of N/P/O-doped HD-HPCs *via* the direct carbonization of multiple-heteroatom-rich hypermolecules. Such a strategy has multiple advantages, including the exclusion of pore-making techniques, activation agents, templates, and complicated and hazard washing processes, demonstrating its green and sustainable properties. The highly active multiple-heteroatom-rich hypermolecular precursors contributed to the formation of abundant micro/mesopores due to the self-abscission of heteroatoms and heteroatom-contiguous carbon atoms at high carbonization temperatures. Consequently, these active structural/compositional features endowed the optimal cathodes with outstanding storage capacities of 139.2 and 88.9 mA h g^{-1} at 0.5 and 20 A g^{-1} for aqueous ZHSCs, respectively. They also delivered a superior storage performance in quasi-solid ZHSCs (QS-ZHSCs) with a high specific capacity of 111.5 mA h g^{-1} at 0.5 A g^{-1}. Superior energy/power densities and long cycling stability were also achieved for aqueous and QS-ZHSCs. The theoretical calculation confirmed the synergetic effects of multiple-atom doping on enhancing the electronic conductivity and reducing the energy barrier between Zn ions and carbon, which promote the Zn-ion adsorption capability. These findings shed fresh light on the straightforward manufacture of superior HD-HPCs for electrochemical energy storage.**

Keywords: molecular engineering, sustainable, hierarchical architecture, heteroatom doping, Zn-ion storage

INTRODUCTION

With the growing demand for sustainable large-scale energy storage devices, the current lithium-ion batteries fail the requirements of safety and environmental friendliness due to their flammable and toxic organic electrolytes [1]. Alternatively, aqueous Zn-based energy storage devices, such as Zn-ion batteries and Zn-ion hybrid supercapacitors (ZHSCs), have emerged as promising power supply systems owing to multiple advantages, such as high theoretical gravimetric/volumetric capacity, low cost ($65/(kW h) for Zn *vs.* $300/(kW h) for Li), appropriate redox potential (−0.76 V), and abundant Zn resources [2]. Moreover, aqueous electrolytes contribute to green and sustainable manufacturing and working conditions. ZHSCs integrated with a battery-type anode and a capacitor-type cathode have received intensive attention due to their relatively high energy and power densities, excellent rate performance, long cycling stability, and high safety [3,4]. Among the verified cathode materials, porous carbons (PCs) are potential for their abundance, environmental friendliness, and structural stability [5]. However, traditionally, commercial activated-carbon (AC) electrodes show an undesirable storage capacity (e.g., <50 mA h g^{-1} at 0.5 A g^{-1}) and a low energy density for ZHSCs, due to their unitary pore structure and insufficient active sites [6,7]. The limited capacitive contribution of the AC cathode is hard to match with the high capacity and kinetics of the Zn anode. Thus, the design and construction of advanced PC cathodes for high-performance ZHSCs face the bottleneck.

Pore engineering and nanostructure design have improved the intrinsic activity of PCs. The development of open-structured PCs with a high specific surface area (SSA) and hierarchical pore channels contributes to abundant active sites and efficient mass transport [8]. Moreover, the nanostructured design and morphological control of nanocarbons boost the effective electrode/electrolyte contact and reduce the ion transport distance, further exposing more active sites for Zn-ion storage. To this end, various structurally engineered PCs, such as hollow carbon nanospheres from MnO_2 nanoflower templates [9], carbon nanowires from MnO_2 nanowire templates [10], three-dimensional PCs from SiO_2 templates [11], K_2CO_3-activated PCs [12], ZnO-activated PCs [2], and a series of alkali-metal-activated PCs [13], have been reported as cathodes for ZHSCs. However, the fabrication processes are generally based on the indirect carbonization of precursors with demands for activations and templates. Fig. 1a summarizes the commonly used activation agents [14]. The addition ratio of raw materials to activation agents is

[1] School of Materials Science and Engineering, Beijing Institute of Technology, Beijing 100081, China
[2] Yangtze Delta Region Academy of Beijing Institute of Technology, Jiaxing 314019, China
[3] School of Aeronautical Engineering, Jiangxi Institute of Economic Administrators, Nanchang 330088, China
[*] Corresponding authors (emails: membrane@bit.edu.cn (Bai Y); chuanwu@bit.edu.cn (Wu C))

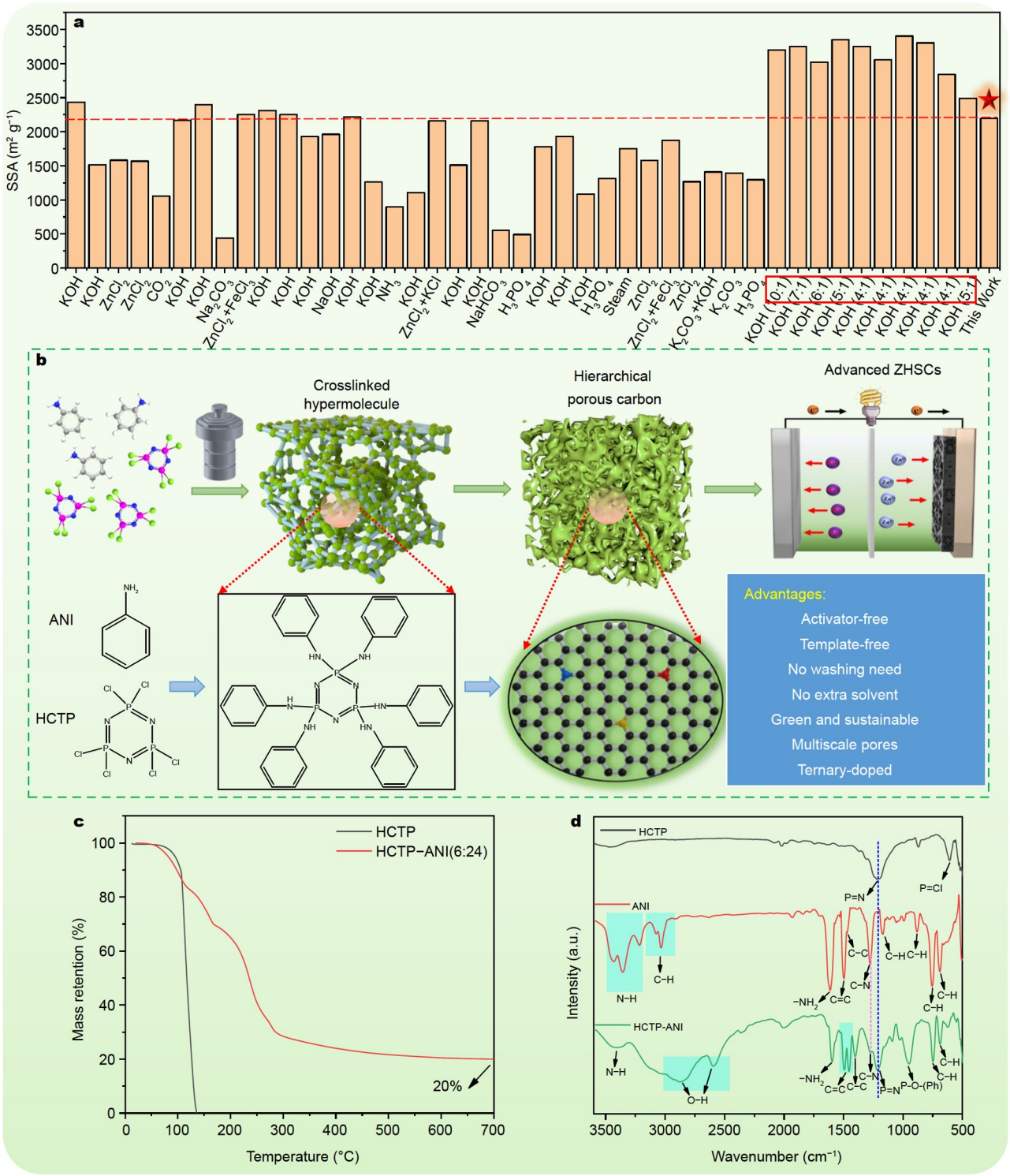

Figure 1 (a) Some representative studies on the fabrication of high SSA carbon materials that required pore activation agents, as summarized in Table S1. (b) Schematic of the fabrication process of N/P/O-PCs. (c) TGA curves under N_2 at a heating rate of 10°C min^{-1}. (d) FTIR spectra of the HCTP, ANI, and HCTP-ANI precursors.

equal to or larger than 1:4 and can reach up to 1:10 [14,15]. The extensive usage of activation agents and templates leads to complicated preparation procedures and time-consuming and hazard washing processes, which fail to balance environmental issues and their targeted electrochemical properties. The involvement of alkali and acid results in the corrosion of devices and difficulties in the recovery and reuse of harmful waste liquids [16,17]. Therefore, green, sustainable, and effective synthesis methods are desired.

On the other hand, heteroatom doping is another efficient strategy to improve the electrochemical activities of PCs by modifying the electronic structure, adsorption barrier, structural

defects, and electrode wettability of carbon materials [18]. Some doping configurations are electrochemically active to contribute pseudocapacities *via* surface faradaic reactions [19]. Currently, single- and multiple-atom-doped PCs have been applied in ZHSCs [5]. For example, the single-atom-doped pyridinic N has been proven to promote Zn-ion storage capacity, due to its high chemical coordination with Zn ions [20]. The N/P dual-atom-doped PCs contributed a high capacity of 164.4 mA h g^{-1} at 0.2 A g^{-1} [9]. The N/S-rich carbon cathode demonstrated a high energy density of 95.9 W h kg^{-1} [10]. The N/B dual-atom-doped carbon nanosheets delivered a specific capacity of 127.7 mA h g^{-1} at 0.5 A g^{-1} [6]. In addition, the P/B and B/S co-doped PCs have been synergistically designed to improve the ZHSC performance [12,19]. Furthermore, multiple N/P/S-doped carbons exhibited a high capacity of 104.7 mA h g^{-1} at 0.1 A g^{-1} [11]. Most heteroatom-doped PCs for ZHSCs are obtained by the uneven combination between carbon resources and dopants, resulting in uncontrollable regulation procedures, arbitrary distribution of heteroatoms, and difficulties in understanding specific heteroatom configurations with Zn-ion storage capability [21]. Moreover, insights into the synergistic effect of multiple-atom-doping on the Zn-ion storage performance are at their early stage. Thus, searching for a sustainable and controllable strategy to engineer carbons with targeted structural and compositional properties and further the in-depth understanding of the structure/composition-performance relationships toward ZHSCs are absolutely imperative.

Molecular engineering based on cooperative interactions between the molecular units provides a promising route to the design of heteroatom-doped hierarchical PCs (HD-HPCs) with accurate control at the molecular level [22,23]. The molecules are usually self-assembled or crosslinked *via* hydrogen or covalent bonding, enabling the regulated composition and pore structure of HD-HPCs by the selection of suitable molecules and specific reactions. For example, metal-organic frameworks with controllable molecular chains and pore-tunable polymer matrix [24,25] and heteroatom-rich conjugated polymers with periodic skeletons (e.g., conjugated polyamides and acrylonitrile copolymers) have been used to fabricate HD-HPCs for ZHSCs [6,26]. However, these frameworks are also obtained from multiple-step construction methods with the assistance of activation and templates. Direct molecular engineering is hard to use in the concurrent realization of HD-HPCs with a high SSA and a hierarchical structure without activation agents or templates [27,28]. To the best of our knowledge, for ZSHCs, a direct molecular engineering strategy for the *in situ* construction of advanced HD-HPCs with integrated multiple-heteroatom doping, high SSA, and hierarchical architectures simultaneously is rarely reported. Such a strategy is very meaningful for the fundamental revelation of the relationship between the optimized structures, doping factors, and Zn-ion storage performances.

Herein, for the first time, we propose the construction of highly active multiple-heteroatom-rich hypermolecules for the sustainable and controllable production of HD-HPCs with high porosity, multiscale pores, and ternary-doped configurations by a direct molecular engineering strategy. The hypermolecule constructed by N/P-rich molecular main chains crosslinked with N-rich branched units can *in situ* realize N/P/O-doped and micro-/mesopore-interconnected PCs (N/P/O-PCs) with a large SSA over 2000 m^2 g^{-1} (Table S1). As summarized in Fig. 1a, such a strategy is green and sustainable without extra hazard activation agents, templates, pore-making techniques, toxic reaction solvents, and high energy consumption. The homogenous multiple doping effect and hierarchical architecture can be concurrently and controllably designed to reveal the structure-performance relationship for ZHSCs. Unlike the reported self-activation mechanisms requiring alkaline and activated blowing agents, the micro/mesopores formed in this work should be ascribed to the uniquely high-active molecular precursors. Heteroatom-rich carbon precursors can be easily activated by KOH agents to exhibit a high porosity due to their less stable carbon structure caused by heteroatom doping effects. Inspired by this condition, this work proposes that constructing a multiple-heteroatom-rich skeleton endows hypermolecular precursors with relatively high activity, enabling the easier formation of nanopores by regulating carbonization schedules. As such, a multiple-heteroatom-rich skeleton with a suitable crosslinking degree and appropriate temperature is necessary. A relatively high temperature combined with highly active hypermolecules contributes to the sufficient self-activation energy for self-abscission of active heteroatoms and self-removing unstable heteroatom-closed carbon atoms from the carbon skeleton, generating massive vacancies or micro/mesopores. The low self-activation energy (low temperature) and high crosslinking degree both result in poorly developed pore structures. For aqueous ZHSCs, the optimized sample delivered an excellent specific capacity of 139.2 mA h g^{-1} at 0.5 A g^{-1} and a high-rate capability of 88.9 mA h g^{-1} at 20 A g^{-1}. The maximum energy density of 107.7 W h kg^{-1} and maximum power density of 17.3 kW kg^{-1} were achieved. The quasi-solid ZHSC (QS-ZHSC) retained a high storage capacity of 111.5 and 62.5 mA h g^{-1} at 0.5 and 20 A g^{-1}, respectively. The aqueous and QS-ZHSCs exhibited long cycling performances. *Ex situ* investigation combined with theoretical calculations confirmed the reversible interactions between the oxygen functional groups and Zn-ion adsorption, and multiple doping synergistically enhanced the electronic conductivity and Zn chemical coordination of the carbon matrix. We believe that such a strategy can be expanded to design carbon materials for different applications that are not limited by ZHSCs.

RESULTS AND DISCUSSION

Fabrication and structure characterization

Fig. 1b shows the fabrication process of N/P/O-PCs, that is, the one-step carbonization of crosslinked hypermolecules assembled by hexachlorocyclotriphosphazene (HCTP) and aniline (ANI). HCTP contains three nitrogen and three phosphorus atoms assembled in an alternating manner to form a cyclic molecular structure, showing an imperative resource for fabricating N/P-doped carbon materials [29]. Moreover, HCTP is easily crosslinked with other functional groups through condensation reactions due to its reactive free chlorines [29]. Molecules with functional groups of –OH or $–NH_2$ are the representative substitution units to couple with HCTP [30,31]. ANI is one of the typical N-rich molecules with $–NH_2$ groups, which are also highly reactive for self-assembly or crosslinking with other substitutes to form hypermolecules [32]. Therefore, HCTP-ANI hypermolecules were constructed for the first time to fabricate HD-HPCs. The pure HCTP without carbon atoms was unstable and easily volatilized during pyrolysis, as evidenced by the zero mass retention according to the thermogravimetric analysis

(TGA) (Fig. 1c). After the co-interaction between HCTP and ANI, the thermal stability significantly improved with a mass retention of 20% (Fig. 1c), confirming the strong crosslinking reaction of the molecular units. Fourier transform infrared (FTIR) spectra were further determined to investigate the interaction between HCTP and ANI (Fig. 1d). Table S2 summarizes the FTIR vibration modes and the corresponding peak positions. For pure HCTP, the characterization absorption peaks at 1211 and 604 cm^{-1} correspond to P–N and P–Cl bonds, respectively [33]. For pure ANI and HCTP-ANI composite, some typical characterization peaks co-exist at around 1600–1612, 1450–1502, 1400–1480, and 1270–1282 cm^{-1}, which correspond to $-NH_2$, C=C, C–C, and C–N bonds, respectively [34,35]. This finding confirms the successful transfer of the functional groups from ANI molecular units to HCTP-ANI. An evident P–N bond peak was also detected in the HCTP-ANI composite, and it belonged to the HCTP units. Moreover, the characterization peak of the P–Cl stretching deformation model was absent in the HCTP-ANI composite, suggesting that the P–Cl bonds in the HCTP were substituted by ANI molecular units [33]. These results confirm the successful condensation polymerization between HCTP and ANI, which generates multiple-heteroatom-rich hypermolecules.

The microstructure of the carbons was investigated by scanning electron microscopy (SEM) (Fig. 2a and Fig. S1). The morphologies of the N/P/O-PCs obtained at different temperatures were generally similar and showed irregular carbon blocks with particle sizes ranging from a few micrometers to hundred micrometers. The transmission electron microscopy (TEM) images (Fig. 2b) confirmed that the amorphous carbons became more ordered with more pronounced graphitic microdomains as the carbonization temperature increased. Moreover, some unregular or uneven pores were observed in the N/P/O-PC-1200 carbon structure, indicating the optimal carbonization temperature for pore formation. A high carbonization temperature induced the rearrangement of carbon atoms and resulted in the collapse of the pore structure and low porosity, accounting for the lack of evident nanopores in the TEM image of N/P/O-PC-1400. Therefore, a temperature of 1200°C ensured that the carbon had a high graphitic crystallite skeleton with excellent electrical conductivity and an optimal porous structure with numerous structural defects. The energy dispersive spectroscopy (EDS) mappings of N/P/O-PC-1200 (Fig. 2c and Fig. S2) showed that C, N, P, and O were homogenously distributed, and this finding indicates the successful ternary doping with N, P, and O atoms into the structure.

The microstructures of N/P/O-PCs were further characterized by X-ray diffraction (XRD) and Raman spectrum. As shown in Fig. 3a, two diffraction peaks at around 2θ = 23° and 44° were detected in the XRD patterns, and they corresponded to the defective or amorphous (002) and graphitic (100) planes of carbon, respectively [36]. As the temperature increased from 800 to 1000°C, the (002) peak generally became narrower and sharper, which suggests the formation of a more ordered structure at high temperatures [37]. At this stage, the low defective structure was attributed to the reduced doping defects, because heteroatoms are unstable at high temperatures [23]. However, the (002) peak position became smaller with a broader and blunter shape at 1200°C, and this result suggests the more defective structure generated in the N/P/O-PC-1200. This finding should be ascribed to the formation of abundant nanopores, which contributes to the rich and intrinsic structural defects in N/P/O-PC-1200, consistent with the TEM results. As the temperature further increased, these intrinsic carbon defects were eventually lost due to the further rearrangement of the carbon layers, leading to a high graphitic degree but the poor pore structure of N/P/O-PC-1400. The Raman spectra (Fig. 3b) showed the presence of two characteristic bands at 1345 and 1585 cm^{-1}, which correspond to the defective structure (D) and graphitic structure (G) bands, respectively [38,39]. The intensity ratio of D/G band (I_D/I_G) showed a decreasing trend when the temperature increased due to the formation of more graphitic domains. These results indicate the optimal temperature of 1200°C for the preparation of PCs in this work.

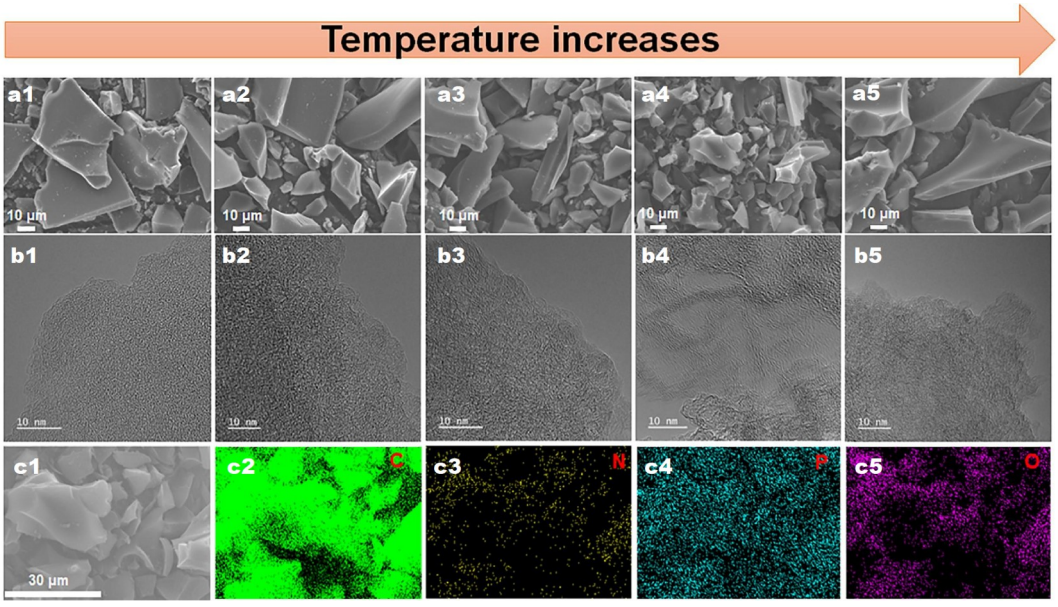

Figure 2 Microstructures of the N/P/O-PCs carbonized from 800 to 1400°C: (a1–a5) SEM images, (b1–b5) TEM images, and (c1–c5) EDS mappings of N/P/O-PC-1200.

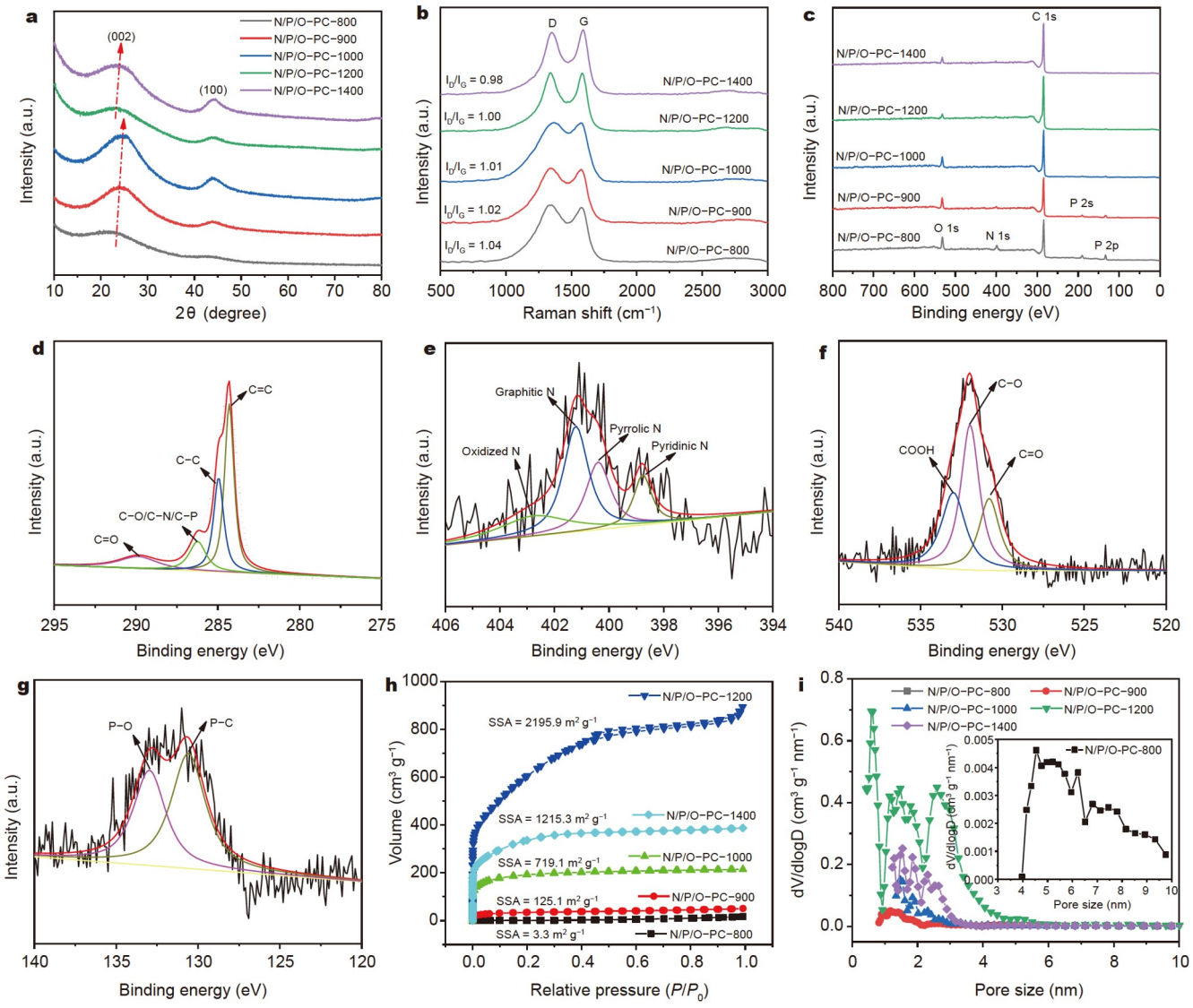

Figure 3 Structure and composition of N/P/O-PCs: (a) XRD pattern, (b) Raman spectra, and (c) full XPS spectra. High-resolution XPS spectra of N/P/O-PC-1200: (d) C 1s, (e) N 1s, (f) O 1s, and (g) P 2p. (h) N_2 adsorption/desorption isotherms and (i) PSD curves of N/P/O-PCs.

X-ray photoelectron spectroscopy (XPS) measurement was carried out to understand the composition of the carbon materials. As shown in Fig. 3c, the total XPS spectra demonstrated the successful doping of N, P, and O heteroatoms into the carbons, suggesting that multiple dopant defects were constructed. The contents of the doped atoms were generally reduced as the annealing temperature increased. Four types of doped C 1s configurations were discovered (Fig. 3d), and they were located at around 284.3, 285.1, 286.3, and 289.8 eV, representing C=C, C–C, C–O/C–N/C–P, and C=O bonds, respectively [7]. The high-resolution N 1s spectrum (Fig. 3e) exhibited that N-doping configurations in N/P/O-PC-1200 can be resolved into pyridinic N at 398.3 eV, pyrrolic N at 400.1 eV, graphitic N at 401.2 eV, and oxidized N at 402.6 eV [25]. The pyridinic and pyrrolic N are good electron-donor configurations that improve the electrochemical activity and electron transfer efficiency of carbon materials, contributing to the improvement of the charge storage performance [40]. The graphitic N configuration can improve the capacitive performance of carbons due to the enhanced electronic conductivity [41]. Three types of oxygen-containing groups, including C=O (530.8 eV), C–O (532.0 eV), and COOH (533.0 eV), can be obtained from the high-resolution O 1s spectrum (Fig. 3f) [42]. Some oxygen-containing groups are electrochemically active and can produce a high pseudocapacity *via* surface faradaic reactions to achieve high-performance carbon electrodes [42]. In addition, oxygen-containing groups are conducive to the electrolyte wettability of the carbon electrodes. The P 2p spectra can be deconvoluted into two peaks (Fig. 3g), including the P–C bond at 130.6 eV and the P–O bond at 133.0 eV [19]. Phosphorus doping can induce the charge distribution of the carbon skeleton to improve its electrical conductivity. In addition, the PCO_3 functional groups in the carbon lattice can improve the electrode-electrolyte wettability [19] to boost the interfacial reaction kinetics. Moreover, multiple doping can further induce synergetic effects on the improvement of electrochemical performance of carbon materials. Table S3 provides additional information on the chemical compositions of carbons under different temperatures.

The pore structure was characterized by N_2 adsorption/desorption measurement. As displayed in Fig. 3h, the samples

(except N/P/O-PC-800) showed typical type-I curves with the capillary condensation of N_2 at the low relative pressure (P) of $P/P_0 < 0.1$, indicating the presence of micropores. Moreover, a significant hysteresis loop existed at the high relative pressure of $0.4 < P/P_0 < 1$ for the N/P/O-PC-1200 sample, demonstrating the formation of abundant mesopores [17]. This observation matches the nanopores discovered in the TEM images. The high adsorbed volume of N_2 at the low relative pressure of N/P/O-PC-1200 confirmed its higher SSA than other samples. The SSA values calculated using the Branauer-Emmett-Teller (BET) method were 3.3, 125.1, 719.1, 2195.9, and 1215.3 $m^2 g^{-1}$ for the samples carbonized from different temperatures. Therefore, N/P/O-PC-1200 owns a more open structure constructed by the interconnected micro-/mesopores with massive intrinsic carbon defects. The pore size distribution (PSD) curves in Fig. 3i also confirm that N/P/O-PC-1200 possessed a multiscale pore structure containing micropores (<2 nm) and mesopores centered at around 3 nm, but only micropore peaks were observed for other samples (extremely low peak intensity for N/P/O-PC-800). Fig. S3 shows the PSD curves of N/P/O-PC-1200 based on Barrett-Joyner-Halenda (BJH) models. Very few mesopores larger than 10 nm existed in N/P/O-PC-1200. Combined with the nonlocal density functional theory (DFT) model, N/P/O-PC-1200 possesses dominated mesopores in the range of 2–5 nm. The hierarchical pore architecture of N/P/O-PC-1200 benefits mass transportation through the realization of high-rate and high-power ZHSCs. More pore information is summarized in Table S4.

Pore formation analysis

Based on the above discussion, an interesting question is how these pores form without any activation agents and pore makers. The reported self-activation mechanisms are generally based on carbon precursors embedded with alkaline elements (such as Na^+, K^+, Zn^{2+}, and Mg^{2+}) [43–46], which can induce the self-activation process during pyrolysis. These self-activation mechanisms are close to the post-activation by chemical activation agents, such as KOH, NaOH, and $ZnCl_2$. Another self-activation mechanism is the direct carbonization of carbon resources and chemical-foaming agents (e.g., urea, melamine, and ammonium chloride) [47–49], which can release vast activation gases (including CO_2, NH_3, and water steam) during pyrolysis. However, no alkaline elements and extra foaming agents were introduced in this study, indicating the unique pore formation mechanism of our molecular engineering strategy.

The reported theoretical calculations point out that N-rich and O-rich precursors are more favorable for KOH activation compared with N-free and O-free precursors [50,51]. The energy barriers of KOH activation for N-rich and O-rich precursors are substantially smaller than those for N-free and O-free precursors, and KOH adsorption positions on the carbon are closer to N and O atoms, showing a higher binding energy between KOH and N-rich and O-rich carbons. Therefore, KOH etching is favored in highly active regions in carbon frameworks [52]. These pioneered studies imply that when molecular precursors have abundant multiple heteroatoms, which leads to a relatively high self-active precursor, highly porous HD-HPCs can possibly be obtained without activation and template agents. The crosslinking structure and degree of the hypermolecular precursor were revealed, and the carbonization schedule determined the microstructure of HD-HPCs [23]. To validate this possibility, scientists should first obtain a multiple-heteroatom-rich crosslinking structure using a rational design. The widely used covalent triazine-based molecules, such as melamine, trichloroisocyanuric acid, trithiocyanuric acid, and HCTP, are potential choices. HCTP not only possesses rich heteroatoms, but is also highly active and can be processed into diverse macromolecules by replacing chlorine atoms with different substitution groups [53]. Therefore, HCTP is regarded as an efficient main chain to realize the high-active multiple-heteroatom-rich skeleton.

Next, a reasonable crosslinking degree enabling an appropriate carbon yield with a high self-activity is necessary for pore formation. To achieve this goal, the crosslinking degree of the HCTP-ANI hypermolecules was regulated by different HCTP dosages. The HCTP was highly active to be volatilized during pyrolysis according to the TGA results. The pure liquid state ANI was also easily volatilized, with the release of vast gases during annealing. Pure ANI-derived carbons have extremely low porosity (e.g., SSA of 18.14 $m^2 g^{-1}$) [54]. After the combination with an increased HCTP dosage, the digital photos (Fig. S4) of the precursors showed an evident state evolution, where a liquid state was observed at a low HCTP addition, and significantly more solid powders were obtained as the HCTP dosage increased. This finding indicates the stronger interaction and higher crosslinking degree of the hypermolecule. As confirmed by the TGA analysis (Fig. S5), the higher HCTP addition (HCTP-ANI-9:24) led to a higher (nearly twice) carbon yield than that of HCTP-ANI-6:24 (the optimal ratio), proving the higher structural stability of HCTP-ANI-9:24 [23]. However, the self-activity of the hypermolecule would be reduced under a high crosslinking degree, leading to a low porosity due to the thermally stable carbon matrix. As confirmed in Fig. 4a, the SSA value of the carbons derived from HCTP-ANI-9:24 was considerably reduced to 1077.6 $m^2 g^{-1}$. The PSD curve also revealed that only micropores dominated the pore structure of the HCTP-ANI-9:24 carbon. These results prove that an optimal crosslinking degree was vital for the rational self-activity of the hypermolecule to obtain a high SSA and a hierarchical pore structure.

Finally, a suitable temperature treatment provides sufficient energy for pore formation. Although HCTP-ANI units were easily volatilized, and the broken bonding configurations can form chemical-foaming gases, their effects on porosity activation were limited. According to the TGA curves (Fig. 1c) and the corresponding mass spectrometry (MS) curves (Fig. 4b–d), the rapid mass loss occurred at below 400°C with the release of vast gases, including NH_3, CH_4, H_2O, CO, O_2, and CO_2, and it represented the chemical blowing stage due to the breakage of unstable bonds. However, the carbons obtained at low temperatures (N/P/O-PC-800 or 900) showed an extremely low porosity, indicating their less influence on pores from gases blowing. The reported gas-blowing agents (e.g., NH_4Cl, melamine, NH_3, and CO_2) can induce a significant porosity at temperatures around 700–900°C [55,56]. Therefore, in our case, foaming gases possibly only induced the formation of large pore channels or cracks during carbonization. According to our molecular engineering strategy, the presence of multiple heteroatoms in hypermolecules results in a high self-activity of the precursor and a less stable carbon structure during pyrolysis. During carbonization, the hypercrosslinked polymers can be processed into a large amount of "duplicate units" with the

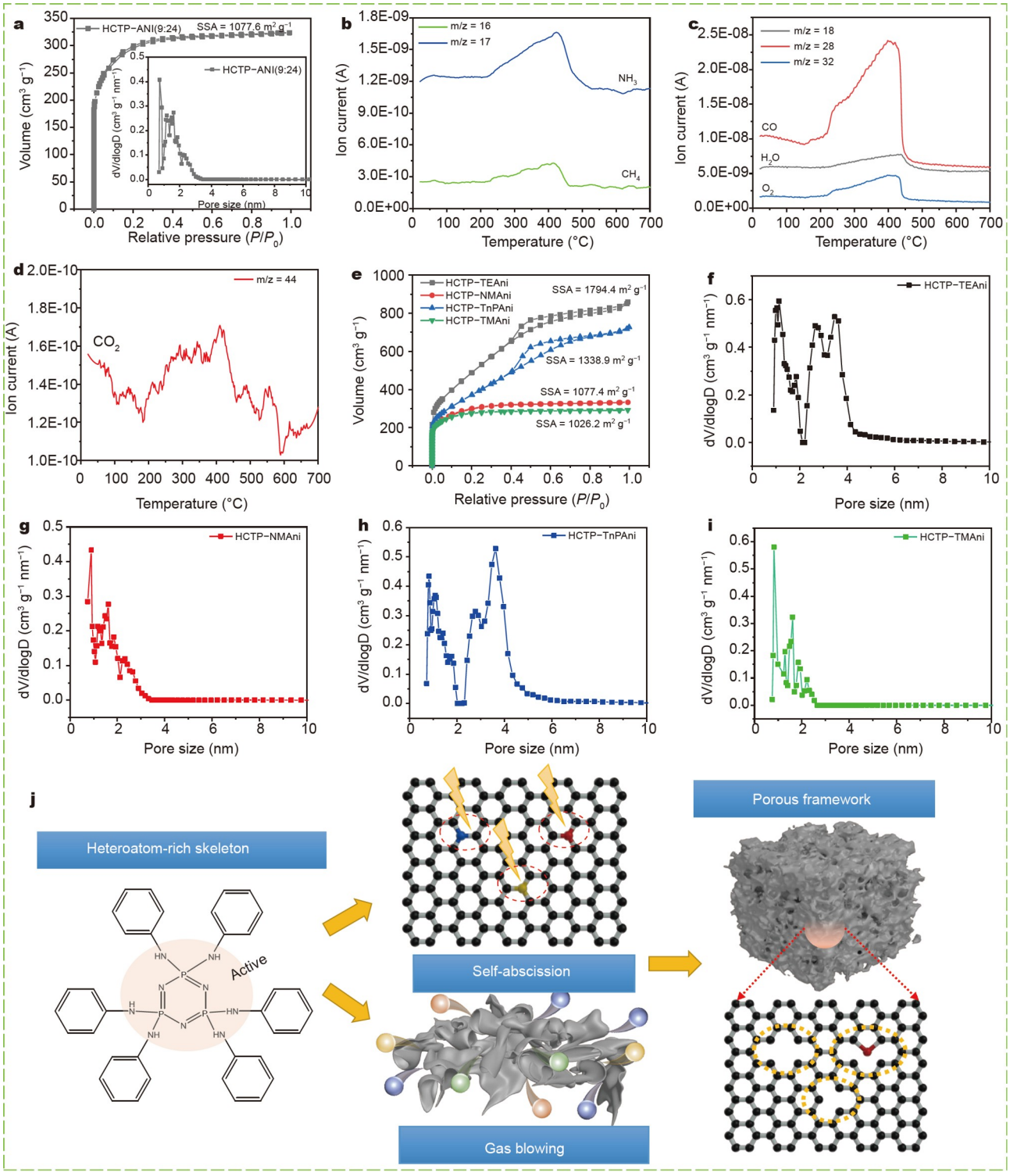

Figure 4 (a) N_2 adsorption/desorption isotherms and PSD curves of the carbon derived from the HCTP-ANI precursor with a high HCTP content. (b–d) TGA corresponding to the MS curves of HCTP-ANI (6:24). (e) N_2 adsorption/desorption isotherms of the carbons derived from crosslinked polymers based on HCTP unit and other molecules, and (f–i) their corresponding PSD curves. (j) Schematic of the pore formation mechanism of the heteroatom-rich skeleton. The samples in (e) are referred to the carbon materials derived from the composites polymierized of HCTP with triethylamine (HCTP-TEAni), HCTP with *N*-methylaniline (HCTP-NMAni), HCTP with tri-*n*-propylamine (HCTP-TnPAni), and HCTP with 2,4,6-trimethylaniline (HCTP-TMAni), respectively.

formation of a meso-/micropore frame, and each unit was constructed by several C–C, C–N, N–H, and N–P bonds, finally forming an interconnected carbon framework [57]. Heteroatoms are easily volatilized and escape from the carbon framework at high temperatures; meanwhile, carbon atoms near heteroatoms are highly active, unstable, and self-removed from the carbon

skeleton at high temperatures [50,51]. The deprivation of heteroatoms and partial carbon atoms leads to the creation of many vacancies or pores on the carbon skeleton. Therefore, a low SSA and high doping level were observed at low annealing temperatures, but a relatively low doping content and high porosity were achieved at higher temperatures. Further increasing the temperature, structural collapse and deformation occurred, leading to low porosity.

To further gain insights into the universality of such a concept, we also investigated different N-containing units during their co-polymerization with HCTP molecules to fabricate HD-HPCs. According to the TGA curves (Fig. S6), the improved mass retention and thermal stability of the composites compared with those of pure HCTP demonstrated the successful formation of the crosslinked hypermolecules from these N-containing units. The EDS mappings (Fig. S7) and XPS spectra (Fig. S8, summarized in Table S5) of these carbons confirmed that N, P, and O were successfully doped into the carbon structure. As shown in Fig. 4e, all the samples showed significant N_2 adsorption quantities at low relative pressures, confirming the microporous structure. HCTP-TEAni and HCTP-TnPAni demonstrated an evident mesoporous structure, as reflected by the significant hysteresis loops at high relative pressures. The PSD curves (Fig. 4f–i) also revealed that micro-/mesopores coexisted in HCTP-TnPAni and HCTP-TEAni, but only micropore-dominated structures were present in HCTP-NMAni and HCTP-TMAni. The SSA values were 1077.38, 1338.86, 1026.25, and 1794.43 $m^2 g^{-1}$. Fig. S9a, b show the PSD curves of HCTP-TnPAni and HCTP-TEAni based on the BJH model, respectively. The mesopores in these two samples were dominant at 2–5 nm, and very few mesopores larger than 10 nm existed. More pore information is summarized in Table S6. The molecular ratio influences the pore formation behavior, and therefore, the relatively low SSA or lack in the hierarchical pore structure of these carbons may be because such a ratio is not the optimal condition for these N-containing units. Therefore, these results were consolidated to determine the unique pore formation mechanism. As illustrated in Fig. 4j, meso/micropore formation is due to the self-abscission of heteroatoms and some heteroatom-contiguous carbon atoms at the atomic level, whereas the gas-blowing effect contributes to the formation of large pore channels.

Electrochemical performance of ZHSCs

We assembled aqueous ZHSCs with N/P/O-PCs as the cathodes, Zn foil as the anodes, and 2.0 mol L^{-1} $ZnSO_4$ solution as the electrolyte. Fig. 5a shows the cyclic voltammetry (CV) curves of Zn//N/P/O-PCs at a scan rate of 30 mV s^{-1}. The CV curves of Zn//N/P/O-PC-1200 showed a considerably plump and rectangular shape with a higher current response and larger integrated area than those of other samples, indicating a better storage performance for N/P/O-PC-1200. Moreover, the near-rectangular shapes of CV curves for Zn//N/P/O-PC-1200 were retained at 400 mV s^{-1} (Fig. 5b), whereas severe distortions were observed in the CV curves for other devices at higher scan rates (Fig. S10), indicating the superior rate performance of the device based on N/P/O-PC-1200. The hierarchical porous structure and higher SSA in N/P/O-PC-1200 secured the efficient mass transfer and effective charge accumulation. Some sub-structures in the CV curve showed small hump peaks at around 1.0/1.2 V, suggesting the presence of certain redox processes. According to the literature, redox processes are possibly related to the faradaic redox reactions between oxygen functional groups and Zn ions, such as –C–OH [58–60], –C=O [13,58], or –COOH [42] ($–C–OH + Zn^{2+} + e^- \rightleftharpoons –C–O–Zn + H^+$; $–C=O + Zn^{2+} + 2e^- \rightleftharpoons –C–O–Zn$; $–COOH + Zn^{2+} + e^- \rightleftharpoons –COO–Zn + H^+$). The galvanostatic charge-discharge (GCD) profiles further reflected the superior storage performance of the Zn//N/P/O-PC-1200 device, which exhibited a high storage capacity (Fig. 5c, d, and Fig. S10). The Zn-ion storage capacities of the Zn//N/P/O-PC-1200 device were 139.2, 118.7, 111.0, 100.1, 98.5, and 88.9 mA h g^{-1} at 0.5, 1.0, 4.0, 6.0, 10.0, and 20.0 A g^{-1} (Fig. 5d), respectively, and these values were better than those of other devices (36/2.8 mA h g^{-1} for Zn//N/P/O-PC-900 and 83.3/10.7 mA h g^{-1} for Zn//N/P/O-PC-1400 at 0.5/10 A g^{-1}) (Fig. 5e). As shown in Fig. S11, the high-loading (5 mg cm^{-2}) device can deliver Zn-ion storage capacities of 125.3, 96.9, 77.5, 59.7, and 40.0 mA h g^{-1} (corresponding to 0.63, 0.48, 0.39, 0.30, and 0.20 mA h cm^{-2}) at 0.2, 0.5, 1.0, 2.0, and 5.0 A g^{-1}, respectively. Compared with the values in Table S7, the specific capacity and rate capability of our Zn//N/P/O-PC-1200 device were comparable to those of most carbon-based ZHSCs. The high specific capacity, excellent rate capability, and wide potential window of the Zn//N/P/O-PC-1200 device contributed to an excellent energy density of 107.7 W h kg^{-1} at a power density of 403.2 W kg^{-1} and an outstanding power density of 17.3 kW kg^{-1} at an energy density of 67.4 W h kg^{-1} (Fig. 5f). These values are comparable to or outperform those of the reported aqueous ZHSCs, such as PPy-750 (107.3 W h kg^{-1} at 214.9 W kg^{-1}) [25], POP-TAPP-NTCA with 48 W h kg^{-1} at 85 W kg^{-1} [61], MCHS with 36.8 W h kg^{-1} at 13.7 kW kg^{-1} [62], ACC with 94 W h kg^{-1} at 68 W kg^{-1} [63], N-HPC with 58.5 W h kg^{-1} at 191 W kg^{-1} [64], N/S-PCD with 106.7 W h kg^{-1} at 160 W kg^{-1} [24], PSC-A with 65.4 W h kg^{-1} at 15.7 kW kg^{-1} [65], WC-6ZnN-12U with 90.9, 83.8, 75.9, 67.1, 53.7, 43.4 W h kg^{-1} at 450, 675, 1125, 2250, 4500, 6750 W kg^{-1} [66], LC with 15 W h kg^{-1} at 360 W kg^{-1} [6], reduced graphene oxide (rGO) with 21.2 W h kg^{-1} at 990 W kg^{-1} [6], and YP-50F with 43.1 W h kg^{-1} at 12 kW kg^{-1} [6]. Moreover, the Zn//N/P/O-PC-1200 device delivered excellent cycling stability, which was reflected by a capacity retention of 97.3% and a stable Coulombic efficiency during the long-term cycling at 1 A g^{-1} (Fig. 5g–i). Moreover, the device can still be stably cycled for 10,000 cycles at 5 A g^{-1} with no evident capacity degradation (Fig. S12). The stable cycling performance is ascribed to the non-significant Zn dendrite formation and robust structural stability of the carbon cathode (in which no structural deformation occurred) (Fig. S13). These results strongly prove the practical potential of the N/P/O-PC-1200 ZHSCs.

To further uncover the reasons for the excellent Zn-ion storage performances, we applied electrochemical impedance spectroscopy (EIS) to study the electronic and ionic transport properties within this system (Fig. 6a). The Nyquist plots contained a straight line at low frequency regions coupled to the semicircle at high-frequency regions, which corresponded to Zn-ion diffusion resistance and charge transfer resistance. N/P/O-PC-1200 showed a smaller semicircle than the others, showing a more favorable charge transfer at the electrode-electrolyte interface. A more vertically straight line was found for N/P/O-PC-1200, confirming the faster Zn-ion transport in the N/P/O-PC-1200 system. This finding also reveals the ideal capacitive behavior of the N/P/O-PC-1200 sample. The calculated equivalent series resistance (ESR) values were 2.96, 2.94, and

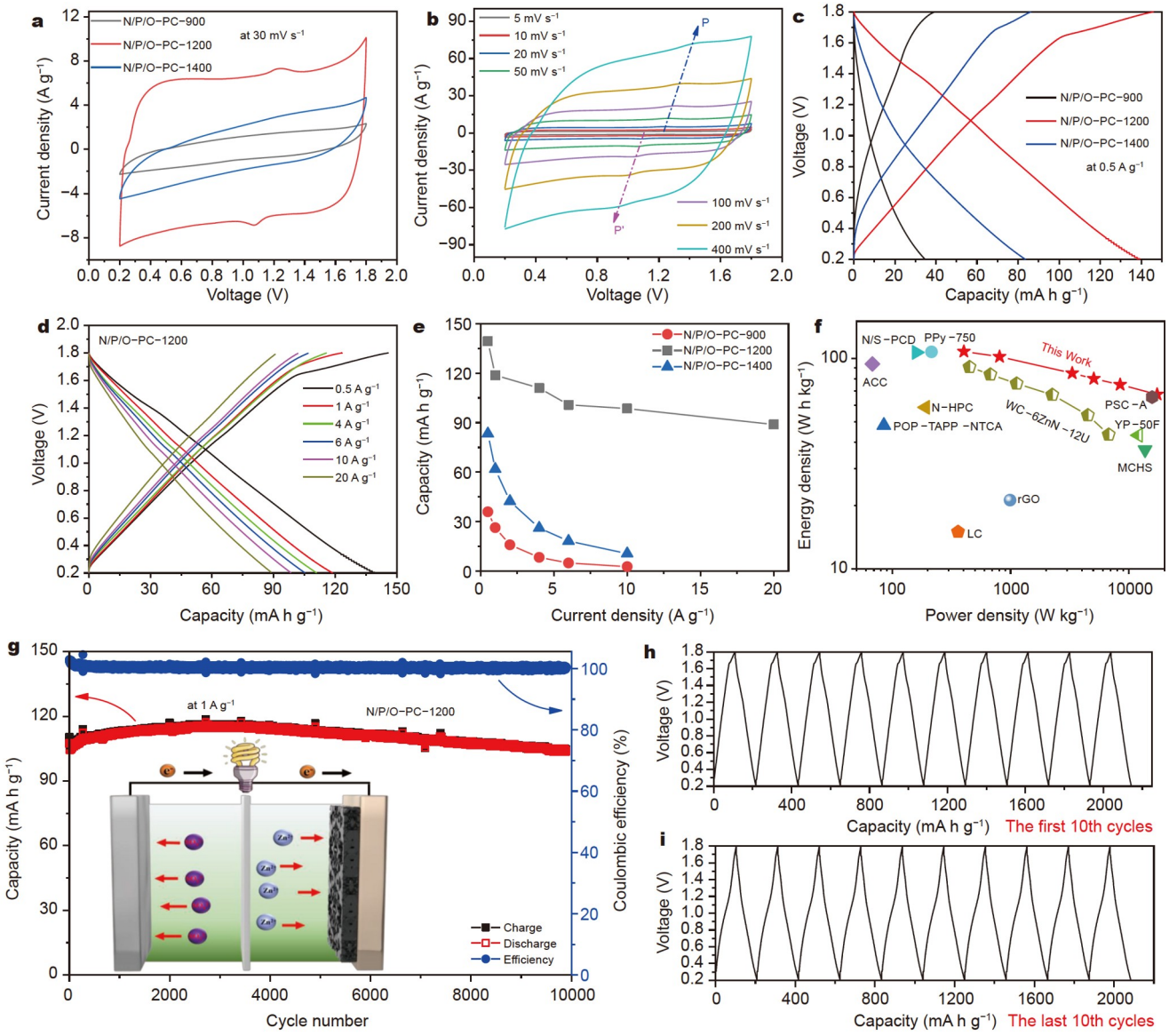

Figure 5 Electrochemical performance of ZHSCs: (a) CV curves at 30 mV s^{-1} for N/P/O-PCs, (b) CV curves of N/P/O-PC-1200 at different scan rates, (c) GCD profiles of N/P/O-PCs at 0.5 A g^{-1}, (d) GCD profiles of N/P/O-PC-1200 at different rates, (e) specific capacities at various rates, (f) Ragone plot, (g) long-term cycling performance at 1 A g^{-1}, and GCD profiles for (h) the first 10 cycles and (i) the last 10 cycles during cycling of the Zn//N/P/O-PC-1200 device.

3.02 Ω for N/P/O-PC-900, N/P/O-PC-1200, and N/P/O-PC-1400, respectively. The low ESR for N/P/O-PC-1200 was ascribed to its high electronic/ionic conductivity due to the high graphitic degree and interconnected hierarchical pore structure. To further reveal the fast electrode kinetics, we further calculated the diffusion coefficient of Zn-ion in the Zn//N/P/O-PC-1200 system from the EIS analysis using the following equations [67]:

$$\omega = 2\pi f, \quad (1)$$

$$Z = R + \sigma\omega^{-1/2}, \quad (2)$$

$$D = 0.5R^2T^2/A^2n^4F^4C^2\sigma^2, \quad (3)$$

where ω is the angular frequency, f is the frequency, Z represents the impedance in the real part, σ is the Warburg coefficient, C is the Zn-ion concentration, R, T, and F are the gas constant, thermodynamic constant, and Faraday constant, respectively, A is the surface area, and n corresponds to the electron transfer number per molecule. Fig. 6b displays the fitted plots regarding the relationship between the real part of the impedance and the low frequencies of the devices. The calculated σ values were 121.79, 17.75, and 56.10 Ω $s^{-1/2}$, and the corresponding Zn-ion diffusion coefficients were 4.00 × 10^{-20}, 1.88 × 10^{-18}, 1.89 × 10^{-19} cm^2 s^{-1} for N/P/O-PC-900, N/P/O-PC-1200, and N/P/O-PC-1400, respectively. Therefore, N/P/O-PC-1200 showed a more desirable ion diffusion efficiency, which was contributed by the hierarchical pore structure, and the hydrophilic surface induced by the N/P/O doping.

The kinetics behaviors of the Zn//N/P/O-PC-1200 device were further investigated by analyzing the CV curves, which can be divided into two parts, namely, the capacitive-controlled contribution and the diffusion-controlled process. According to the power-law equation [6]:

$$i = av^b, \quad (4)$$

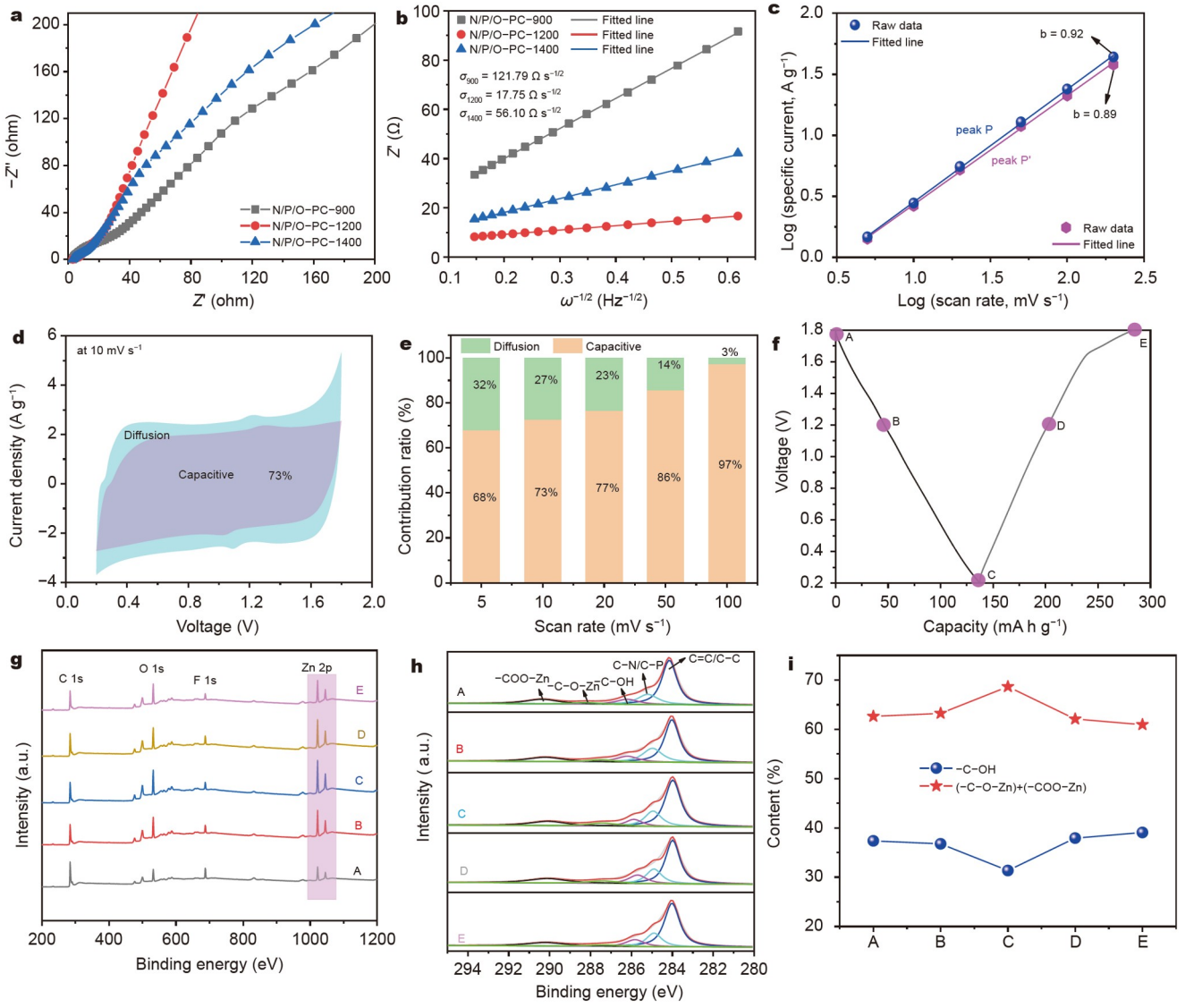

Figure 6 (a) Nyquist plots. (b) Relationship between the real part impedance and low frequency. (c) Fitting plots of log(*i*) *versus* log(*v*) of the device. (d) Capacitive and diffusion contributions to the total current from CV analysis at 10 mV s^{-1}. (e) Capacitive and diffusion contribution ratios at different scan rates. (f) Selected voltage points in the GCD curves of the N/P/O-PC-1200 cathode at 0.5 A g^{-1} for *ex situ* characterization. (g) *Ex situ* full XPS spectra at the selected states. (h) *Ex situ* C 1s XPS spectra at the selected states. (i) Intensity ratios of –C–OH and (–C–O–Zn) + (–COO–Zn) peaks according to (h).

where *i* (A g^{-1}) is the total current, *v* (mV s^{-1}) is the scan rate, and *a* and *b* are adjustable parameters. The value of *b* can be calculated based on the slope of the fitting linear log(*i*)-log(*v*) relationship. Fig. 6c displays the fitted plots of the selected peaks in the CV curves. The calculated *b* values of the anodic and cathodic peaks (as marked in Fig. 6c) were 0.92 and 0.89, respectively, indicating that both capacitive- and diffusion-controlled processes contributed to the total storage capacity, and the capacitive-controlled process was predominant. The detailed capacity contribution ratios of these processes were quantitatively determined by the following equation [6]:

$$i = k_1 v + k_2 v^{1/2}, \quad (5)$$

where k_1 and k_2 are the constant parameters at a specific scan rate, and they can be obtained by plotting the relationship curves of $i/v^{1/2}$ and $v^{1/2}$, respectively, to evaluate the capacity contribution. As shown in Fig. 6d, the calculated capacitive contribution ratio at 10 mV s^{-1} was 73%. Fig. 6e further demonstrates the capacitive-dominant behavior and fast electrochemical kinetics at high scan rates.

To investigate the Zn-ion storage mechanism in the N/P/O-PC-1200 cathode, we implemented *ex situ* XPS spectra to gain insights into the evolution of the surface chemical states of the N/P/O-PC-1200 cathode at different states of charge. The Zn//N/P/O-PC-1200 device was first charged to 1.8 V (marked A state) from the open-circuit voltage (around 1.3 V), discharged to 1.2 V as state B, fully discharged to 0.2 V as state C, and then recharged to 1.2 V (state D) and full charge state E (Fig. 6f). As shown in Fig. 6g, the Zn 2p intensity gradually increased and reached the maximum value at state C, indicating Zn-ion adsorption on the N/P/O-PC-1200 cathode surface during discharge. The lower Zn 2p intensity during the recharging process suggested the desorption process of Zn ions from the cathode. From the high-resolution C 1s spectra (Fig. 6h), five config-

urations at 284.3, 285.8, 286.1, 287.3, and 290.1 eV can be divided, and they corresponded to the C=C/C–C, C–N/C–P, –C–OH, –C–O–Zn, –COO–Zn bonds, respectively [42,58]. The presence of –C–O–Zn and –COO–Zn bonding components indicated the near-faradaic reactions between the Zn ions and C–OH/C=O groups [42]. The evolution of the intensity ratios of –C–OH peak and (–C–O–Zn) + (–COO–Zn) peaks was analyzed and displayed in Fig. 6i. The (–C–O–Zn) + (–COO–Zn) peak ratios increased from stage A to stage C upon discharge and decreased from stage C to stage E during recharge, confirming the reversible faradaic charge storage mechanism between the Zn ions and oxygen-containing groups [42,58].

The reversible reaction process was further investigated by *ex situ* XRD, Raman, SEM, and EDS analysis measurements. According to the XRD patterns of different discharge/charge stages (Fig. S14a), the diffraction peaks related to zinc hydroxide sulfate hydrate were observed at B, C, and D stages and disappeared at the full charge E stage, showing the reversible formation and dissolution of $Zn_4SO_4(OH)_6{\cdot}xH_2O$ [58–60]. This event was also evidenced by the SEM images (Fig. S15), where the zinc hydroxide sulfate hydrate nanoflakes gradually formed and disappeared from stages A to E. EDS mappings (Fig. S16) further revealed the same content evolution of O and Zn, that is, their increment during discharge and decrement during charge. The formation of zinc hydroxide sulfate hydrates was ascribed to the proton insertion into the carbon cathode while leaving OH^- behind and causing pH increment at the low-potential region [13]. Therefore, these results also reflected the reversible proton (de)insertion at the cathode [68]. The structural evolution of the carbon cathode was further evaluated by Raman spectra (Fig. S14b). The I_D/I_G ratios of the cathode gradually increased during discharge and returned to normal values at the full charge stage, implying the reversible transformation of the disordered structure of the carbon cathode [13]. The XRD patterns (Fig. S17) of the Zn anode at different stages only showed similar locations of diffraction peaks that corresponded to the (002),

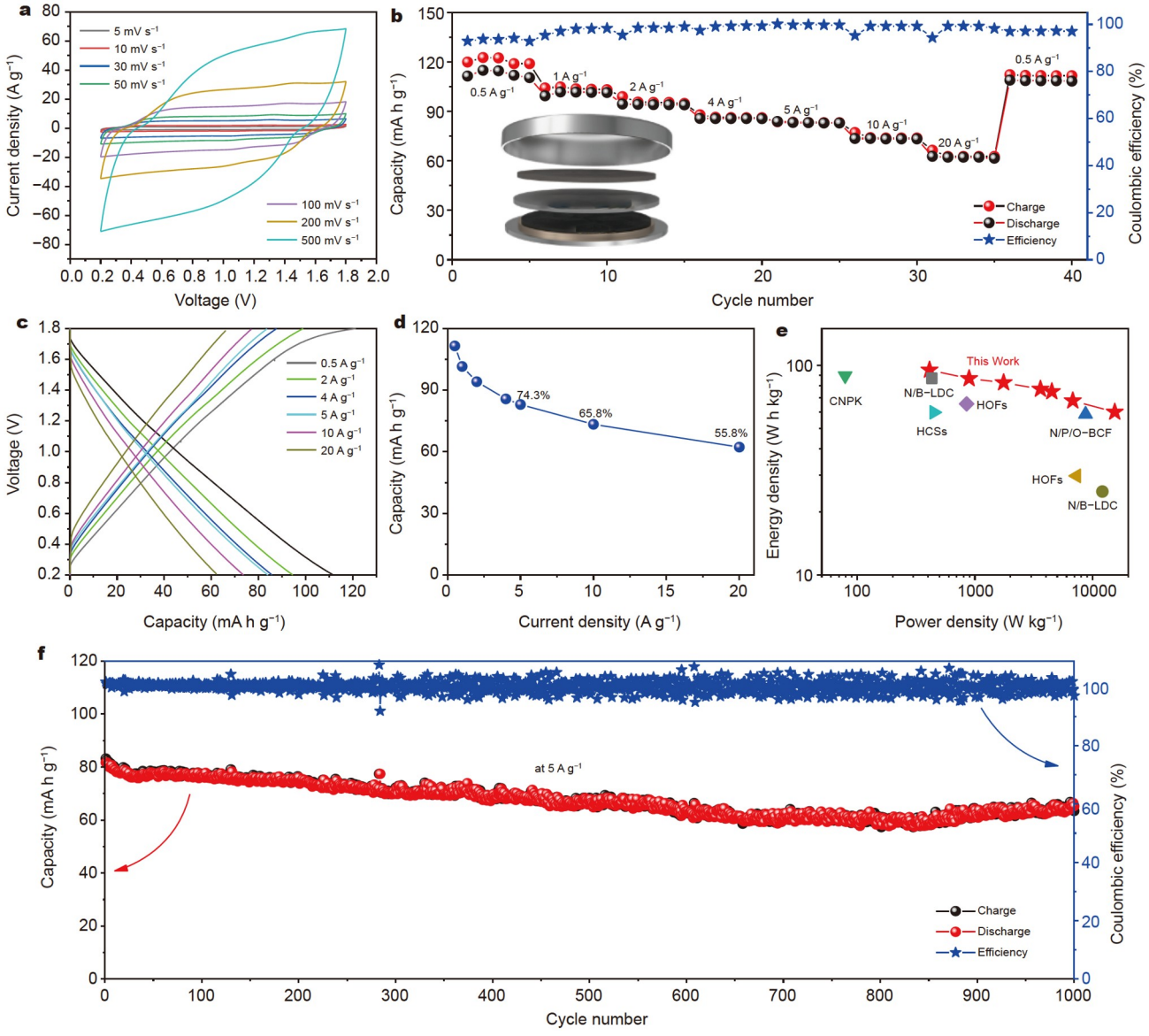

Figure 7 Electrochemical performance of QS-ZHSCs: (a) CV curves, (b) cycling test, (c) GCD profiles, (d) specific capacity at different rates; (e) Ragone plot with comparisons; (f) long-term cycling performance.

(100), (101), (102), and (103) planes of Zn (PDF: 04-0813), implying the reversible stripping-deposition conversion of Zn with nearly no byproduct formation on the Zn surface [69]. This finding is consistent with the *ex situ* SEM results, as shown in Fig. S18, in which the Zn surface experienced a rough morphology with a low amount of nanosheets at different stages. Therefore, these results proved the highly reversible reaction processes during the charge/discharge of the ZHSCs.

To demonstrate the feasibility of the N/P/O-PC-1200 cathodes in practical applications, we further built a QS-ZHSC using gelation/$ZnSO_4$ gel as the electrolyte. The open-circuit voltage after the self-discharge test (Fig. S19) for 3600 min was 1.139 V. Thus, the corresponding self-discharge rate can be calculated as R_{SD} = (1.8 − 1.139)/60 = 11.02 mV h^{-1}. The ratio of the remaining discharge capacity *versus* the charge capacity was 76.8%. The regular rectangle-like CV curves (Fig. 7a) demonstrated that the energy storage performance of the Zn//N/P/O-PC-1200 QS-ZHSC was comparable to that of aqueous ZHSCs. The well-retained current response at a high scan rate of 500 mV s^{-1} showed an excellent rate performance. As further confirmed by GCD measurements (Fig. 7c), this device exhibited well-developed triangle-like GCD profiles at high current densities, revealing its superior rate performance. Fig. 7b, d display the specific capacities under different current densities. An outstanding specific capacity of 111.5 mA h g^{-1} was obtained at 0.5 A g^{-1}, and values of 82.8, 73.4, and 62.2 mA h g^{-1} were retained at 5, 10, and 20 A g^{-1}, respectively, corresponding to capacity retentions of 74.3%, 65.8%, and 55.8%. The superior rate capability should be ascribed to the hierarchical pore structure and high electrical conductivity for efficient ion/electron transfer. From the above data, the calculated maximum energy density of this device was 95.05 W h kg^{-1} at a power density of 411.3 W kg^{-1}, and the maximum power density was 15.4 kW kg^{-1} at an energy density of 59.89 W h kg^{-1}. As shown by the result in Fig. 7e, the energy and power densities of the Zn//N/P/O-PC-1200 QS-ZHSC were comparable to or better than those of previously reported carbon-based QS-ZHSCs, such as N/B-LDC with 86.8 W h kg^{-1} at 429.6 W kg^{-1} (25 W h kg^{-1} at 12.1 kW kg^{-1}) [6], N/B/O-BCF (58.5 W h kg^{-1} at 8.7 kW kg^{-1}) [38], CNPK (89.3 W h kg^{-1} at 79 W kg^{-1}) [70], HOFs-derived

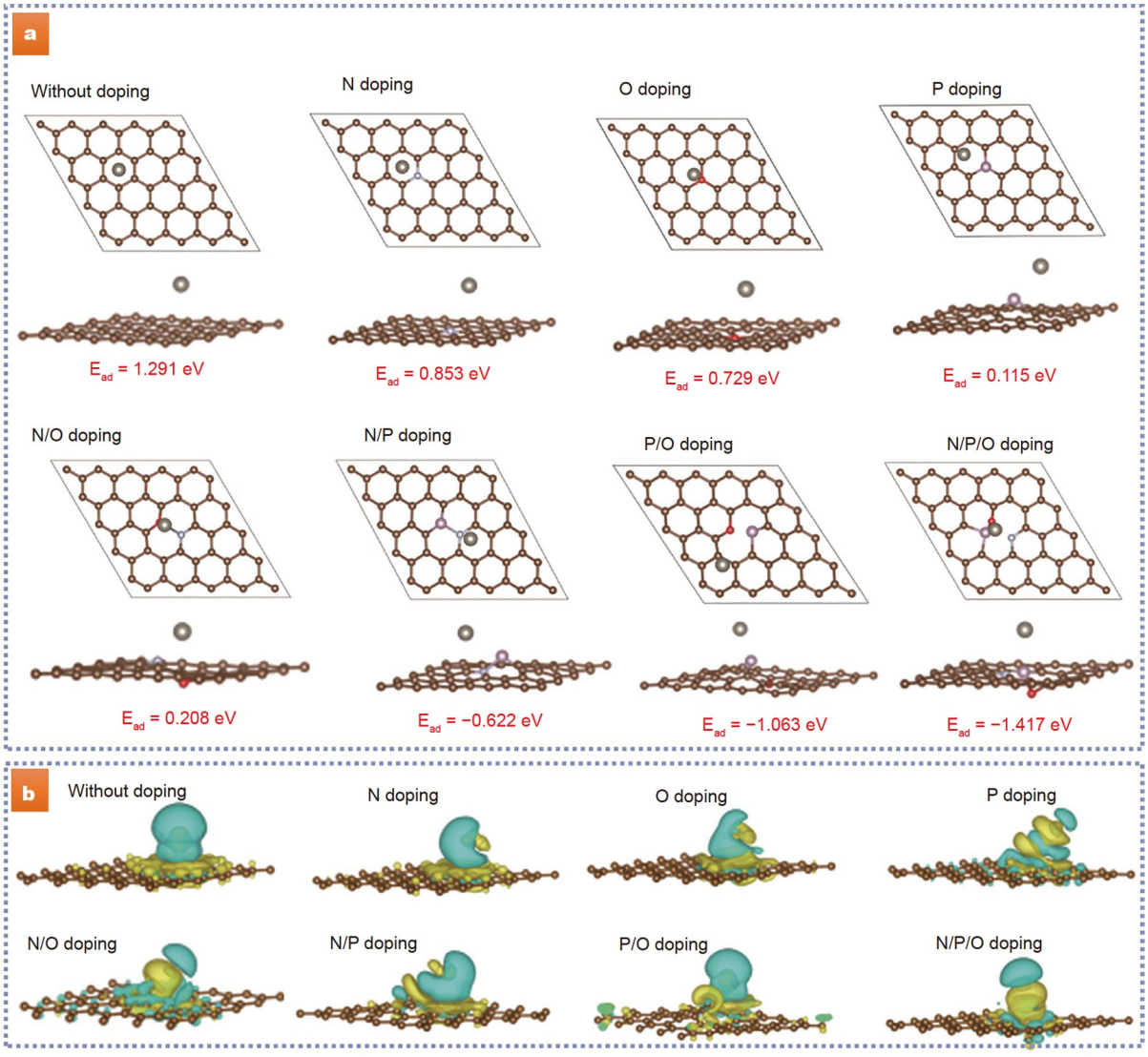

Figure 8 (a) Simulated graphene models with different doping configurations and the corresponding adsorption energies of the Zn ions on these model structures. (b) Differential charge density of the above model structures with different doping configurations.

carbon with 65.5 W h kg^{-1} at 850 W kg^{-1} (29.7 W h kg^{-1} at 7.3 kW kg^{-1}) [71], and HCSs (59.7 W h kg^{-1} at 447.8 W kg^{-1}) [72]. Importantly, this device still exhibited 65.4 mA h g^{-1} at 5 A g^{-1} with nearly 100% Coulombic efficiency after 1000 cycles (Fig. 7f), corresponding to a capacity retention as high as 80%. The capacity degradation for such QS-ZHSC is unlikely due to the Zn and carbon electrodes, and it was reflected by the non-significant dendrite formation and absence of structural deformation in the Zn anode and carbon cathode (Fig. S20), respectively. The instability of the gelatin-based gel electrolyte under an acidic environment during charge and discharge may be responsible for the receding capacity [73]. More information is discussed in Supplementary information in Fig. S20.

To reveal the influence of heteroatom doping on the Zn-ion storage performance, we performed DFT calculations to understand the adsorption and interaction between the Zn ions and the carbon matrix. The undoped carbon, single-atom-doped carbons, binary-doped carbons, and ternary-doped carbon models were optimized to calculate the relative adsorption energy (ΔE_{ad}) values of Zn atom (Fig. 8a). Compared with the pristine carbon, heteroatom-doped carbons showed significantly lower ΔE_{ad} values, indicating a stronger interaction between the Zn atom and doped carbons. Moreover, the ΔE_{ad} values of the carbons significantly decreased from single-doping to ternary doping configurations, confirming the synergistic adsorption effect induced by multiple-atom doping [9,19]. It could be assigned to the high electron richness of N/P/O doping which favors the adsorption of Zn-ion to improve the storage performance. Fig. 8b shows the charge density difference diagram of different carbon models after Zn-ion adsorption. Heteroatom doping modified the electronic structure of the models. In all cases, a net gain of electronic charge can be observed between the Zn atom and the carbon matrix, showing that charge depletion and accumulation mainly occurred on Zn and heteroatom adsorption sites [9]. This finding indicates the charge transferred from the adsorbed Zn-ion to its nearest neighboring C atoms. The charge transferred to the bonding carbon atoms in the heteroatom-doped structure, and the charge accumulation was close to the heteroatom-doped sites [74]. This result also confirms that the heteroatom-doped carbons possessed a stronger interaction between the Zn ions and the carbon matrix. The heteroatom-doped carbon provides a fast electron transfer pathway to promote Zn-ion adsorption. Therefore, N/P/O doping induces a high affinity between Zn and carbon and improves the electronic conductivity of carbon, contributing to excellent Zn-ion storage performance.

CONCLUSION

In summary, we successfully provided an innovative molecular engineering strategy for the design of advanced HD-HPCs based on the simple pyrolysis of multiple-heteroatom-rich hypermolecules. Given the high activity of the molecular precursor, heteroatoms and carbon atoms adjacent to heteroatoms are easily detached from the carbon matrix to form abundant pores. Such an activation-free and template-free molecular engineering strategy contributed to the sustainable and controllable fabrication of HD-HPCs with multiple advantages. The structure-performance relationship was comprehensively established. Consequently, the N/P/O-ternary-doped, meso-/microporous carbon materials with a large SSA of 2195.9 m^2 g^{-1} were obtained, and they showed excellent storage performance for aqueous and QS-ZHSCs. High specific capacity (139.2/111.5 mA h g^{-1} at 0.5 A g^{-1}), excellent rate capability (88.9/62.2 mA h g^{-1} at 20 A g^{-1}), and high power and energy densities (107.7 W h kg^{-1}/17.3 kW kg^{-1}, 95.05 W h kg^{-1}/15.4 kW kg^{-1}) were achieved for aqueous ZHSCs and QS-ZHSCs. The ZHSCs also exhibited long cycling stability. Moreover, the synergistic mechanisms of N/P/O doping on the enhancement of Zn-ion storage performance were theoretically investigated, and the results showed that ternary doping improved the electronic conductivity and promoted the chemical adsorption of Zn ions, resulting in superior storage capacity. Therefore, this work not only paves the way for the sustainable design of advanced PC materials, but also offers insights into the Zn-ion storage mechanism.

Received 25 April 2022; accepted 30 June 2022; published online 21 September 2022

1 Ni Q, Kim B, Wu C, *et al.* Non-electrode components for rechargeable aqueous zinc batteries: Electrolytes, solid-electrolyte-interphase, current collectors, binders, and separators. Adv Mater, 2022, 34: 2108206
2 Shang P, Liu M, Mei Y, *et al.* Urea-mediated monoliths made of nitrogen-enriched mesoporous carbon nanosheets for high-performance aqueous zinc ion hybrid capacitors. Small, 2022, 18: 2108057
3 Wu L, Dong Y. Recent progress of carbon nanomaterials for high-performance cathodes and anodes in aqueous zinc ion batteries. Energy Storage Mater, 2021, 41: 715–737
4 Wu F, Liu M, Li Y, *et al.* High-mass-loading electrodes for advanced secondary batteries and supercapacitors. Electrochem Energ Rev, 2021, 4: 382–446
5 Liu Q, Zhang H, Xie J, *et al.* Recent progress and challenges of carbon materials for Zn-ion hybrid supercapacitors. Carbon Energy, 2020, 2: 521–539
6 Lu Y, Li Z, Bai Z, *et al.* High energy-power Zn-ion hybrid supercapacitors enabled by layered B/N co-doped carbon cathode. Nano Energy, 2019, 66: 104132
7 Deng X, Li J, Shan Z, *et al.* A N, O co-doped hierarchical carbon cathode for high-performance Zn-ion hybrid supercapacitors with enhanced pseudocapacitance. J Mater Chem A, 2020, 8: 11617–11625
8 Li X, Wang Y, Zhao Y, *et al.* Graphene materials for miniaturized energy harvest and storage devices. Small Struct, 2022, 3: 2100124
9 Li J, Zhang J, Yu L, *et al.* Dual-doped carbon hollow nanospheres achieve boosted pseudocapacitive energy storage for aqueous zinc ion hybrid capacitors. Energy Storage Mater, 2021, 42: 705–714
10 Li J, Yu L, Wang W, *et al.* Sulfur incorporation modulated absorption kinetics and electron transfer behavior for nitrogen rich porous carbon nanotubes endow superior aqueous zinc ion storage capability. J Mater Chem A, 2022, 10: 9355–9362
11 Shang K, Liu Y, Cai P, *et al.* N, P, and S co-doped 3D porous carbon-architectured cathode for high-performance Zn-ion hybrid capacitors. J Mater Chem A, 2022, 10: 6489–6498
12 Zhang X, Zhang Y, Qian J, *et al.* Synergistic effects of B/S co-doped spongy-like hierarchically porous carbon for a high performance zinc-ion hybrid capacitor. Nanoscale, 2022, 14: 2004–2012
13 Wang L, Peng M, Chen J, *et al.* High energy and power zinc ion capacitors: A dual-ion adsorption and reversible chemical adsorption coupling mechanism. ACS Nano, 2022, 16: 2877–2888
14 Huang J, Liang Y, Hu H, *et al.* Ultrahigh-surface-area hierarchical porous carbon from chitosan: Acetic acid mediated efficient synthesis and its application in superior supercapacitors. J Mater Chem A, 2017, 5: 24775–24781
15 Yuan G, Huang W, Guan K, *et al.* A universal KOH-free strategy towards nitrogen-doped carbon nanosheets for high-rate and high-energy storage devices. J Mater Chem A, 2019, 7: 26469–26478
16 Fu R, Yu C, Li S, *et al.* A closed-loop and scalable process for the production of biomass-derived superhydrophilic carbon for supercapacitors. Green Chem, 2021, 23: 3400–3409

17 Liu M, Huo S, Xu M, *et al.* Structural engineering of N/S co-doped carbon material as high-performance electrode for supercapacitors. Electrochim Acta, 2018, 274: 389–399
18 Feng X, Bai Y, Liu M, *et al.* Untangling the respective effects of heteroatom-doped carbon materials in batteries, supercapacitors and the ORR to design high performance materials. Energy Environ Sci, 2021, 14: 2036–2089
19 Lee YG, An GH. Synergistic effects of phosphorus and boron co-incorporated activated carbon for ultrafast zinc-ion hybrid supercapacitors. ACS Appl Mater Interfaces, 2020, 12: 41342–41349
20 Li Y, Lu P, Shang P, *et al.* Pyridinic nitrogen enriched porous carbon derived from bimetal organic frameworks for high capacity zinc ion hybrid capacitors with remarkable rate capability. J Energy Chem, 2021, 56: 404–411
21 Fan M, Yuan Q, Zhao Y, *et al.* A facile "double-catalysts" approach to directionally fabricate pyridinic N–B-pair-doped crystal graphene nanoribbons/amorphous carbon hybrid electrocatalysts for efficient oxygen reduction reaction. Adv Mater, 2022, 34: 2107040
22 He L, Li WC, Xu S, *et al.* Molecular-based design of microporous carbon nanosheets. Chem Eur J, 2019, 25: 3209–3218
23 Liu M, Wu F, Zheng L, *et al.* Nature-inspired porous multichannel carbon monolith: Molecular cooperative enables sustainable production and high-performance capacitive energy storage. InfoMat, 2021, 3: 1154–1170
24 Yang Y, Chen D, Wang H, *et al.* Two-step nitrogen and sulfur doping in porous carbon dodecahedra for Zn-ion hybrid supercapacitors with long term stability. Chem Eng J, 2022, 431: 133250
25 Zhu X, Guo F, Yang Q, *et al.* Boosting zinc-ion storage capability by engineering hierarchically porous nitrogen-doped carbon nanocage framework. J Power Sources, 2021, 506: 230224
26 Zheng X, Miao L, Song Z, *et al. In situ* nanoarchitecturing of conjugated polyamide network-derived carbon cathodes toward high energy-power Zn-ion capacitors. J Mater Chem A, 2022, 10: 611–621
27 Wang H, Shao Y, Mei S, *et al.* Polymer-derived heteroatom-doped porous carbon materials. Chem Rev, 2020, 120: 9363–9419
28 Puthusseri D, Aravindan V, Madhavi S, *et al.* 3D micro-porous conducting carbon beehive by single step polymer carbonization for high performance supercapacitors: The magic of *in situ* porogen formation. Energy Environ Sci, 2014, 7: 728–735
29 Kale VS, Hwang M, Chang H, *et al.* Microporosity-controlled synthesis of heteroatom codoped carbon nanocages by wrap-bake-sublime approach for flexible all-solid-state-supercapacitors. Adv Funct Mater, 2018, 28: 1803786
30 Yang S, Cao C, Sun Y, *et al.* Nanoscale magnetic stirring bars for heterogeneous catalysis in microscopic systems. Angew Chem Int Ed, 2015, 54: 2661–2664
31 Mohanty P, Kull LD, Landskron K. Porous covalent electron-rich organonitridic frameworks as highly selective sorbents for methane and carbon dioxide. Nat Commun, 2011, 2: 401
32 Kuznetsov AN, Ayupov AB, Yeletsky PM, *et al.* Influence of monomer content on course of aniline polymerization in presence of high surface area carbon. J Electroanal Chem, 2019, 835: 73–80
33 Liu S, Cheng X, He Z, *et al.* Amine-terminated highly cross-linked polyphosphazene-functionalized carbon nanotube-reinforced lignin-based electrospun carbon nanofibers. ACS Sustain Chem Eng, 2020, 8: 1840–1849
34 Ginic-Markovic M, Matisons JG, Cervini R, *et al.* Synthesis of new polyaniline/nanotube composites using ultrasonically initiated emulsion polymerization. Chem Mater, 2006, 18: 6258–6265
35 Dhibar S, Bhattacharya P, Hatui G, *et al.* Transition metal doped poly (aniline-*co*-pyrrole)/multi-walled carbon nanotubes nanocomposite for high performance supercapacitor electrode materials. J Alloys Compd, 2015, 625: 64–75
36 Li H, Wu J, Wang L, *et al.* A zinc ion hybrid capacitor based on sharpened pencil-like hierarchically porous carbon derived from metal-organic framework. Chem Eng J, 2022, 428: 131071
37 Yu K, Wang X, Yang H, *et al.* Insight to defects regulation on sugarcane waste-derived hard carbon anode for sodium-ion batteries. J Energy Chem, 2021, 55: 499–508
38 Fan H, Hu X, Zhang S, *et al.* Flower-like carbon cathode prepared *via in situ* assembly for Zn-ion hybrid supercapacitors. Carbon, 2021, 180: 254–264
39 Zhou Z, Zhou X, Zhang M, *et al. In situ* two-step activation strategy boosting hierarchical porous carbon cathode for an aqueous Zn-based hybrid energy storage device with high capacity and ultra-long cycling life. Small, 2020, 16: 2003174
40 Liu M, Li X, Shao C, *et al.* Synchronous-ultrahigh conductive-reactive N-atoms doping strategy of carbon nanofibers networks for high-performance flexible energy storage. Energy Storage Mater, 2022, 44: 250–262
41 Wang Z, Wang X, Bai Y, *et al.* Developing an interpenetrated porous and ultrasuperior hard-carbon anode *via* a promising molten-salt evaporation method. ACS Appl Mater Interfaces, 2020, 12: 2481–2489
42 Shao Y, Sun Z, Tian Z, *et al.* Regulating oxygen substituents with optimized redox activity in chemically reduced graphene oxide for aqueous Zn-ion hybrid capacitor. Adv Funct Mater, 2021, 31: 2007843
43 Zhang J, Wu D, Zhang Q, *et al.* Green self-activation engineering of metal-organic framework derived hollow nitrogen-doped carbon spheres towards supercapacitors. J Mater Chem A, 2022, 10: 2932–2944
44 Dai J, Wang L, Xie A, *et al.* Reactive template and confined self-activation strategy: Three-dimensional interconnected hierarchically porous N/O-doped carbon foam for enhanced supercapacitors. ACS Sustain Chem Eng, 2020, 8: 739–748
45 Hou L, Yang W, Jiang B, *et al.* Intrinsic defect-rich porous carbon nanosheets synthesized from potassium citrate toward advanced supercapacitors and microwave absorption. Carbon, 2021, 183: 176–186
46 Yu K, Zhao H, Wang X, *et al.* Hyperaccumulation route to Ca-rich hard carbon materials with cation self-incorporation and interlayer spacing optimization for high-performance sodium-ion batteries. ACS Appl Mater Interfaces, 2020, 12: 10544–10553
47 Zhang H, Zhang Z, Luo JD, *et al.* A chemical blowing strategy to fabricate biomass-derived carbon-aerogels with graphene-like nanosheet structures for high-performance supercapacitors. ChemSusChem, 2019, 12: cssc.201900267
48 Wang Y, Xuan H, Lin G, *et al.* A melamine-assisted chemical blowing synthesis of N-doped activated carbon sheets for supercapacitor application. J Power Sources, 2016, 319: 262–270
49 Ai W, Wang X, Zou C, *et al.* Molecular-level design of hierarchically porous carbons codoped with nitrogen and phosphorus capable of *in situ* self-activation for sustainable energy systems. Small, 2017, 13: 1602010
50 Han P, Cheng M, Luo D, *et al.* Selective etching of C–N bonds for preparation of porous carbon with ultrahigh specific surface area and superior capacitive performance. Energy Storage Mater, 2020, 24: 486–494
51 Zhang S, Li X, Zhou J, *et al.* The critical role of oxygen-containing functional groups in the etching behavior of activators to carbon materials. ACS Sustain Chem Eng, 2021, 9: 1646–1655
52 Yao L, Wu Q, Zhang P, *et al.* Scalable 2D hierarchical porous carbon nanosheets for flexible supercapacitors with ultrahigh energy density. Adv Mater, 2018, 30: 1706054
53 Wan C, Huang X. Cyclomatrix polyphosphazenes frameworks (cyclo-POPs) and the related nanomaterials: Synthesis, assembly and functionalisation. Mater Today Commun, 2017, 11: 38–60
54 Li P, Zhang D, Xu Y, *et al.* Nitrogen-doped hierarchical porous carbon from polyaniline/silica self-aggregates for supercapacitor. Chin J Chem Eng, 2019, 27: 709–716
55 Mohan D, Pittman Jr. CU. Activated carbons and low cost adsorbents for remediation of tri- and hexavalent chromium from water. J Hazard Mater, 2006, 137: 762–811
56 Luo W, Wang B, Heron CG, *et al.* Pyrolysis of cellulose under ammonia leads to nitrogen-doped nanoporous carbon generated through methane formation. Nano Lett, 2014, 14: 2225–2229
57 Lu Y, Liang J, Deng S, *et al.* Hypercrosslinked polymers enabled micropore-dominant N, S co-doped porous carbon for ultrafast electron/ion transport supercapacitors. Nano Energy, 2019, 65: 103993
58 Fan W, Ding J, Ding J, *et al.* Identifying heteroatomic and defective sites in carbon with dual-ion adsorption capability for high energy and

power zinc ion capacitor. Nano-Micro Lett, 2021, 13: 59
59 Yin J, Zhang W, Wang W, *et al.* Electrochemical zinc ion capacitors enhanced by redox reactions of porous carbon cathodes. Adv Energy Mater, 2020, 10: 2001705
60 Zhang H, Liu Q, Fang Y, *et al.* Boosting Zn-ion energy storage capability of hierarchically porous carbon by promoting chemical adsorption. Adv Mater, 2019, 31: 1904948
61 Cui FZ, Liu Z, Ma DL, *et al.* Polyarylimide and porphyrin based polymer microspheres for zinc ion hybrid capacitors. Chem Eng J, 2021, 405: 127038
62 Liu P, Liu W, Huang Y, *et al.* Mesoporous hollow carbon spheres boosted, integrated high performance aqueous Zn-ion energy storage. Energy Storage Mater, 2020, 25: 858–865
63 He L, Liu Y, Li C, *et al.* A low-cost Zn-based aqueous supercapacitor with high energy density. ACS Appl Energy Mater, 2019, 2: 5835–5842
64 Liu P, Gao Y, Tan Y, *et al.* Rational design of nitrogen doped hierarchical porous carbon for optimized zinc-ion hybrid supercapacitors. Nano Res, 2019, 12: 2835–2841
65 Li Z, Chen D, An Y, *et al.* Flexible and anti-freezing quasi-solid-state zinc ion hybrid supercapacitors based on pencil shavings derived porous carbon. Energy Storage Mater, 2020, 28: 307–314
66 Lou G, Pei G, Wu Y, *et al.* Combustion conversion of wood to N, O co-doped 2D carbon nanosheets for zinc-ion hybrid supercapacitors. Chem Eng J, 2021, 413: 127502
67 Liu M, Wu F, Bai Y, *et al.* Boosting sodium storage performance of hard carbon anodes by pore architecture engineering. ACS Appl Mater Interfaces, 2021, 13: 47671–47683
68 Xu H, He W, Li Z, *et al.* Revisiting charge storage mechanism of reduced graphene oxide in zinc ion hybrid capacitor beyond the contribution of oxygen-containing groups. Adv Funct Mater, 2022, 32: 2111131
69 Peng Z, Guo J, He Q, *et al.* Hierarchically nitrogen-doped mesoporous carbon nanospheres with dual ion adsorption capability for superior rate and ultra-stable zinc ion hybrid supercapacitors. Sci China Mater, 2022, 65: 2401–2411
70 Zhang H, Chen Z, Zhang Y, *et al.* Boosting Zn-ion adsorption in cross-linked N/P co-incorporated porous carbon nanosheets for the zinc-ion hybrid capacitor. J Mater Chem A, 2021, 9: 16565–16574
71 Fan H, Zhou S, Li Q, *et al.* Hydrogen-bonded frameworks crystals-assisted synthesis of flower-like carbon materials with penetrable meso/macropores from heavy fraction of bio-oil for Zn-ion hybrid supercapacitors. J Colloid Interface Sci, 2021, 600: 681–690
72 Chen S, Ma L, Zhang K, *et al.* A flexible solid-state zinc ion hybrid supercapacitor based on co-polymer derived hollow carbon spheres. J Mater Chem A, 2019, 7: 7784–7790
73 Jo YJ, Kwon KY, Khan ZU, *et al.* Gelatin hydrogel-based organic electrochemical transistors and their integrated logic circuits. ACS Appl Mater Interfaces, 2018, 10: 39083–39090
74 Lv C, Xu W, Liu H, *et al.* 3D sulfur and nitrogen codoped carbon nanofiber aerogels with optimized electronic structure and enlarged interlayer spacing boost potassium-ion storage. Small, 2019, 15: 1900816

Acknowledgements This work was supported by the National Natural Science Foundation of China (21975026), the Science and Technology Program of Guangdong Province (2020B0909030004), and the Graduate Interdisciplinary Innovation Project of Yangtze Delta Region Academy of Beijing Institute of Technology (Jiaxing, GIIP2021-002).

Author contributions Bai Y and Wu C proposed the research idea. Liu M, Bai Y, and Wu C designed the project and performed the experiments. Liu M performed the material fabrication, characterization, and battery testing. Feng X and Wang Y participated in material fabrications, data analyses, and schematic illustrations. Zheng L and Li X performed the theoretical calculations and data analysis. Li Y and Gong Y provided technique support, data analyses, and scientific discussions. Wu F, Bai Y, and Wu C supervised the research. Liu M, Bai Y, and Wu C wrote the manuscript. All authors discussed the results and commented on the manuscript.

Conflict of interest The authors declare that they have no conflict of interest.

Supplementary information Experimental details and supporting data are available in the online version of the paper.

Mingquan Liu is currently a PhD candidate under the supervision of Prof. Feng Wu at the School of Materials Science and Engineering, Beijing Institute of Technology (BIT). His research interests focus on the structural engineering of carbon materials for supercapacitors and sodium-ion batteries.

Feng Wu is currently a professor at BIT. He is the director of the Green Energy Research Institute. As the chief scientist, he has undertaken studies on new secondary batteries and related energy materials for a long time.

Ying Bai is currently a professor at BIT. She earned her bachelor's degree from Harbin Institute of Technology, China, in 1997. She completed her PhD degree at the School of Chemical Engineering and Materials Science, BIT in 2003. Her research interests focus on the electrochemical energy storage and conversion technology.

Chuan Wu is a professor at BIT. He received his PhD degree in applied chemistry from BIT in 2002, followed by a 2-year postdoctoral fellowship at Dalian Institute of Chemical Physics, Chinese Academy of Sciences. His interests are new energy materials and secondary batteries based on multielectron materials.

分子工程化可持续制备多元素掺杂的分级多孔碳材料用于高性能锌离子存储

刘明权[1,2], 吴锋[1,2], 冯鑫[1], 王亚辉[1,2], 郑路敏[1], 李新[3], 李莹[1], 巩玉腾[1], 白莹[1*], 吴川[1,2*]

摘要 具备低价、优异倍率性能、长寿命、高安全性的水系锌离子混合电容器(ZHSCs)是理想的下一代能量存储器件. 高比表面积、多级孔、富缺陷的掺杂分级多孔碳(HD-HPCs)是非常有前景的ZHSCs正极材料. 但是, 可持续且可控原位构筑同时具备多种结构组分优势的HD-HPCs仍然面临挑战. 本文提出一种新的分子工程化策略, 即直接碳化富含多种异质原子的超分子前驱体, 便可实现原位构筑多元掺杂HD-HPCs. 该绿色可持续策略具有多种优势, 包括不需要额外的成孔技术、活化剂、模板剂、以及复杂且危险的清洗过程. 由于富杂原子超分子前驱体具有较高的活性, 高温碳化过程中杂原子以及邻近杂原子的碳原子很容易从碳骨架中脱离, 形成丰富的微介孔结构. 因此, 活性结构与组分优化后的正极材料在水系ZHSCs中0.5和20 A g^{-1}下容量分别达到139.2和88.9 mA h g^{-1}, 在准固态ZHSCs中0.5 A g^{-1}下容量也能够达到111.5 mA h g^{-1}. 此外, 水系和准固态ZHSCs也具备高能量和功率密度, 以及长循环稳定性. 理论计算表明多原子掺杂能够协同提升碳材料的导电性, 且降低锌离子与碳之间的相互作用能垒, 因而提升锌离子的吸附性能. 本工作为直接制备HD-HPCs及其电化学储能应用提供了新思路.

